



CHAPTER IV

INORGANIC MESOPOROUS MEMBRANE FOR POTENTIALLY USED IN PROTON EXCHANGE MEMBRANE

4.1 Abstract

Inorganic Mesoporous Membranes are a new alternative to improve high-temperature fuel cell performance in proton exchange membrane fuel cells (PEMFCs) to substitute for Nafion. They possess high porosity and high specific surface areas, resulting in high proton conductivity. In this study, niobium-modified titania and antimony/niobium-modified titania ceramic were prepared via the sol-gel technique. The various contents of antimony, 0 to 3 wt%, and 3% niobium are incorporated into titania to improve the porous surface condition of the ceramic particles. The xerogels were heated at about 500°C. Inorganic membranes were fabricated by using the spin-coating technique using epoxy resin as a binder. The physical, chemical, and electrical properties of these membranes were investigated. The XRD and Raman results showed that pure TiO₂ and doped TiO₂ nanoparticles obtained possess an anatase structure with mesoporosity. The specific surface area of the doped TiO₂ was higher than that of pure TiO₂ and it is worth pointing out that the doping of antimony affected the surface areas more than the doping of niobium in TiO₂. Moreover, these membranes were also tested to evaluate their potential use as an electrolyte in PEMFCs by using impedance spectroscopy, TGA, universal testing machine and water uptake. The results showed that the proton conductivity value of TiO₂/epoxy membrane was enhanced by doping niobium and antimony into TiO₂ matrix and all of the nano-composite films present good thermal and mechanical properties.

KEYWORDS: PEMFCs Sol-gel process Niobium-modified Titanium dioxide
Antimony/Niobium-modified Titanium dioxide

4.2 Introduction

In the present, conventional proton exchange membrane fuel cells (PEMFCs) use Nafion as the electrolyte. Nafion is the trademark (produced by DuPont) of perfluorosulfonic polymers, composed of carbon-fluorine backbone chains and perfluoro side chains with sulfonic acid ion-exchange groups. It can show excellent proton conductivity due to the presence of water molecules in its structure. However, it is expensive and the loss of proton conductivity of Nafion at temperature above 80°C can be occurred due to the lower-water content, resulting in the decrease of cell performance. In the practice, successful membranes should have many properties such as non-fluorinated membrane, high chemical and mechanical stability at elevated temperature, and good performance at low relative humidity (R.H.). They should also be impermeable to H₂ and O₂. In addition, they must be easily synthesized from available and low-cost starting materials.

The development of new polymer system is one of the choices in order to improve its high-temperature performance. These membranes are made with various organic polymers. However, this choice is not suitable for application in electrochemical processes because of their low specific surface area and environment-dependent structure. Therefore, scientists are turning to new alternative that is the synthesis and development of total inorganic membranes such as TiO₂ [1, 2, 3], SiO₂ and ZrO₂ that possess high proton conductivity, accompanied by good chemical and thermal stability, high porosity, and high specific surface areas (Inorganic Mesoporous Membrane). Moreover, these materials may be deposited on electrode better than that of polymer membranes. Furthermore, an inorganic membrane process is also simpler and more economical than other methods, as compared with organic membranes.

For practical use in fuel cells, the electrolyte materials may be in form of flexible and gas-tight thick film. For this reason, great interest has been focused on the development of inorganic/organic hybrid membranes such as Nafion-TiO₂ [4, 5, 6], Nafion-SiO₂ [7], poly (fluorinated aromatic ethers)-SiO₂ [8] and Nafion-ZrO₂ [5, 9]. Inorganic membranes can be modified by using polymer as binder in order to improve mechanical properties of membranes since the organic part brings

membrane elastic and hydrophobic properties and the inorganic component gives high proton conductivity along with hydrophilic properties. Therefore, inorganic/organic composites, which are applicable at higher temperature and in moderate water vapor pressures, are suitable for electrolyte application.

In the present study, inorganic particles, including titanium dioxide, niobium-modified titanium dioxide and antimony/niobium modified titanium dioxide particle, were prepared by the sol-gel method. This method offers a sharper pore-size distribution in the final product, compared to polymeric sol-gel method. The control of pore structure is very important for designing the proton conducting paths. Later, various inorganic membranes were prepared by the spin coating technique, using epoxy resin as a binder. The resulting membranes should provide high proton conductivity at temperature above 80 °C, high mechanical, thermal and chemical stability.

4.3 Experimental

4.3.1 Materials

Titanium (IV) butoxide, niobium (V) chloride and antimony (V) chloride were purchased from Aldrich Chemical Co. Inc. (USA). Glacial acetic acid and methanol were purchased from Lab-Scan Company Co.Ltd. Epotec[®] epoxy resin and Epotec[®] curing agent were supplied from Aditya Birla Chemicals (Thailand) Ltd. (Epoxy Division). All chemicals were used as received.

4.3.2 Equipment

The Raman spectrum was measured by a laser Raman Spectrometer (Renishaw-1000) at an output power of 200 mW of 1064 nm Nd:YAG laser. Characterization of crystal structure of products were obtained from a Rigaku X-ray diffractometer (XRD) system equipped with a RINT 2000 wide angle goniometer and a Cu tube for generating a CuK α 1 radiation ($\lambda = 1.54 \text{ \AA}$) was used to obtain the X-ray diffraction patterns at a generator voltage of 40 kV and a generator current of 30 mA. Nickel filter was used as the K β filter. The goniometer parameters were divergence slit = 1° (2 θ); scattering slit = 1° (2 θ); and receiving slit = 0.3 nm.

Sample was spread on a glass slide. A scan speed of $5^\circ (2\theta)/\text{min}$ with a scan step of $0.02^\circ (2\theta)$ was used during a continuous run in the 20° to $80^\circ (2\theta)$ range. The scanning electron micrographs were carried out to identify the microstructure of a sample. The samples were characterized using a JEOL JSM-6400 scanning electron microscope (SEM) and the doped Nb and Sb species were identified by LINK ISIS series 300 for energy dispersive X-ray (EDX) analysis. Transmission electron microscopy (TEM) was carried out using a Model H-7650 Transmission Electron Microscope apparatus, operating at 100 kV with a 0.204 nm point resolution. Thermo gravimetric analysis was carried out on a Perkin-Elmer TG-DTA pyris diamond over 30° - 900°C at a heating rate of $10^\circ\text{C}/\text{min}$ under nitrogen atmosphere. Nitrogen adsorption-desorption isotherms at 77 K were obtained using Thermo Finnigan, Sorptomatic 1990 from Quanta Chrom Company. The Brunauer-Emmet-Teller (BET) equation was used to calculate the specific surface area. Pore size distributions were obtained using the Barret-Joyner-Halenda (BJH) model in the range of mesopores and the Horvath-Kawazoe approach for micropore determinations. Lloyd Universal Testing machine Model LRX was carried out to measure the mechanical properties of the thin films following ASTM D882. Electrochemical fuel cell test station was carried out to evaluate the potential use as electrolyte in PEMFC. Electrochemical tests were carried out in a 25 cm^2 commercial single cell supplied by Electrochem connected to a Fuel Cell Technologies work station. Membrane-electrode-assemblies with the different membranes were tested in a range of $25^\circ\text{C} < T < 100^\circ\text{C}$ in humidified. The proton conductivity of films samples was measured by four-probe electrochemical impedance spectroscopy (EIS) using a Solartron 1260 frequency response analyzer and a Solartron 1287 potentiostat. The outer electrodes are connected to the working and counter electrodes on the 1287 potentiostat, and the two inner electrodes are connected to the reference electrodes.

4.3.3 Sol-gel Processing of Antimony-modified Titania Ceramics

Titanium (IV) butoxide ($\text{Ti}(\text{OC}_4\text{H}_9)_4$) was dissolved in the mixture between methanol/acetic acid ratio at room temperature with continuous stirring. The ratios of methanol/acetic acid were varied. In a different beaker, 3 wt.% antimony (V) chloride (SbCl_5) was dissolved in methanol and gradually mixed with TiO_2 sol.

After that, the gel was calcined at temperature about 500 °C, 3 hours. Antimony-modified titania particles were ground into powder and then sieved by mesh#325. TiO₂ powder was also prepared in order to use it as a reference to compare with other. The ceramic powder was characterized using Raman, XRD, TEM, SEM and EDX. The surface area and pore size distribution were also measured using Nitrogen sorption.

4.3.4 Sol-gel Processing of Antimony and Niobium-modified Titania

Ceramics

Titanium (IV) butoxide (Ti(OC₄H₉)₄) was dissolved in the mixture between methanol/acetic acid ratio at room temperature with continuous stirring. The ratios of methanol/acetic acid were varied. In different beakers, 3 wt.% Niobium (V) chloride was dissolved in methanol and 0-3 wt.% antimony (V) chloride (SbCl₅) was dissolved in methanol in the other one and then gradually mixed with TiO₂ sol respectively. After that, the gel was calcined at temperature about 500 °C, 3 hours. Antimony and niobium-modified titania particles were ground into powder and then sieved by mesh#325. TiO₂ powder was also prepared in order to use it as reference to compare with other. The ceramic powder was characterized using Raman, XRD, TEM, SEM and EDX. The surface area and pore size distribution were also measured using Nitrogen sorption.

4.3.5 Preparation of Ceramic Membranes by The Spin Coating Technique

Epoxy resin, hardener and 70 wt.% ceramic powder were mixed together and then the thin films were fabricated by the spin coating technique at room temperature. The thickness of thin film was adjusted by varying the speed of spin coating and the coating time. The mould was then transferred in a vacuum oven for initial curing process at temperature of 35 °C for 1 h to evacuate the entrapped air. Based on the visual observation and the homogenous color of sample, minimum sedimentation occurred in the sample. The mixture was then placed into the oven for curing process followed by cooling at room temperature. The dispersion of ceramic particles was observed by using SEM. The ceramic membranes were tested in order to evaluate the potential use as electrolyte in PEMFCs at high temperature by using

TGA, Impedance spectroscopy, Water uptake and Lloyd Universal Testing machine were carried out to measure the mechanical properties of the thin films.

4.3.6 Membrane Electrode Assembly Preparation and Accelerated Fuel Cell Life Test

The loading of Pt/C catalyst on the anode and cathode are $0.25 \text{ mg Pt cm}^{-2}$, respectively. Two electrodes with effective area 25 cm^2 were hot-pressed to one piece of membrane to form a MEA. The MEA was mounted in a single cell with stainless steel end plates and stainless steel mesh flow field as current collectors. The accelerated fuel cell life tests were performed via the open-circuit voltage (OCV) test. During the OCV tests, H_2 and air with saturated humidity were fed to the anode and the cathode, respectively.

4.4 Results and discussion

4.4.1 XRD Analysis of Pure and doped TiO_2 Particles

The crystal structure of pure and doped TiO_2 particles was examined by XRD. All of the samples were calcined at 500°C for 3 h in a furnace and the diffractograms shown in Fig.4.1 indicate that all of the samples possess an anatase phase and no peaks of rutile and mixed phases were found.

Table 4.1 Summary of Physical Properties of TiO_2 and doped TiO_2 Samples

Samples	Crystal size, D (nm)	$d_{(hkl)}$	Lattice parameter		Experimental 2θ position of 1 0 1 peak
			a (Å)	c (Å)	
TiO_2	15.0425	3.5146	3.78	9.51	25.32
3 wt%Sb- TiO_2	10.1721	3.5173	3.79	9.51	25.30
3 wt%Nb- TiO_2	14.4030	3.5173	3.79	9.50	25.30
3 wt%Nb-1 wt%Sb- TiO_2	15.0377	3.5173	3.79	9.50	25.30
3 wt%Nb-2 wt%Sb- TiO_2	13.8385	3.5228	3.79	9.52	25.26
3 wt%Nb-3 wt%Sb- TiO_2	13.2964	3.5201	3.79	9.50	25.28

The anatase peaks were indexed as (101), (004), (200), (105), (211), (204), (116), (220) and (215) in the order of increasing diffraction angles, indicating a body centered tetragonal crystalline structure of TiO_2 crystal [10]. It also shows that the increase of the full width at half-maximum (FWHM) of the XRD peaks with doping antimony and niobium exhibits the decrease of grain size, as reported in Table 4.1.

The grain sizes of the TiO_2 and doped TiO_2 powders were calculated using the Scherrer equation [11]. It is worth noting that the doping of antimony deviate crystal size more than the doping of niobium in TiO_2 . This may be due to the more difference of ionic radius between titanium (IV) and antimony (V). The crystal size of doped particles decreased with the increase of Sb dopant. The size reduction is attributed to the suppression of crystal growth by an introduction of Sb dopant into TiO_2 crystal [12].

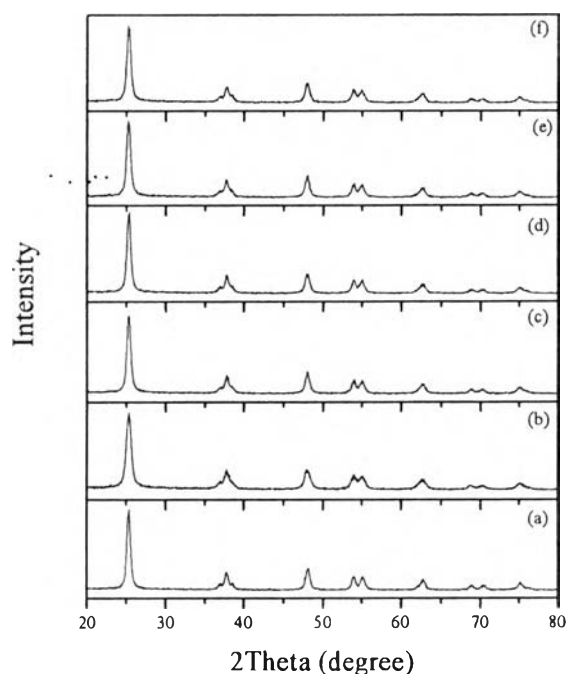


Figure 4.1 XRD patterns for (a) TiO_2 , (b) 3 wt% Sb-TiO_2 , (c) 3 wt% Nb-TiO_2 , (d) 3wt% $\text{Nb-1wt}\%$ Sb-TiO_2 , (e) 3wt% $\text{Nb-2wt}\%$ Sb-TiO_2 , (f) 3wt% $\text{Nb-3wt}\%$ Sb-TiO_2 which all of these was calcined at 500°C .

The doping of antimony and niobium atoms into the TiO_2 lattice does not give any significant changes in the diffractograms. The lattice parameters a and c ,

as listed in Table 4.1, were calculated based on Bragg's law ($2d \sin\theta = \lambda$) and a formula for a tetragonal system [13],

$$\frac{l}{d^2} = \frac{h^2 + k^2}{a^2} + \frac{l^2}{c^2}$$

There is no considerable difference in the lattice parameters of doped materials, this suggests that the structure of doped TiO₂ samples was not changed or distorted from anatase structure of pure TiO₂.

4.4.2 Raman Spectra of TiO₂ and Doped TiO₂ Particles

The X-ray diffraction studies revealed the anatase structure of the pure and doped TiO₂ particles. The formation of the anatase structure was further confirmed by the Raman spectroscopy studies, which showed almost all of the expected vibrational modes of anatase TiO₂ in Fig. 4.2. The peaks observed at around 143, 200, 392, 513 and 635 cm⁻¹ were attributed to the anatase phase of TiO₂ [14].

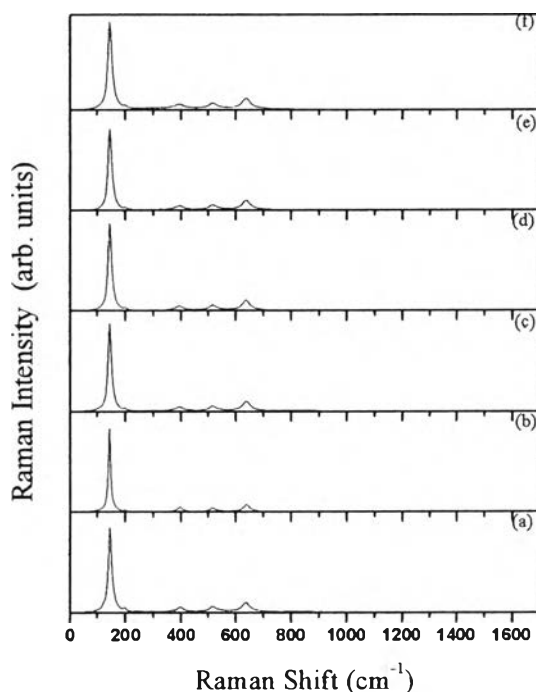


Figure 4.2 Raman spectra of (a) TiO₂, (b) 3 wt% Sb-TiO₂, (c) 3 wt% Nb-TiO₂, (d) 3 wt% Nb-1 wt% Sb-TiO₂, (e) 3 wt% Nb-2 wt% Sb-TiO₂, (f) 3 wt% Nb-3 wt% Sb-TiO₂ which all of these was calcined at 500 °C.

Within the allowed experimental error of a few wave numbers (instrumental error bar), there is no significant shift in the Raman peaks with doping antimony and niobium into TiO₂. This confirms that the anatase structure is remained for the entire range of antimony and niobium doping TiO₂. This result is in agreement with the X-ray diffraction studies. The absence of the characteristic vibrational modes of Nb or Nb₂O₅ and Sb or Sb₂O₅ in the Raman spectra reveals that no Nb₂O₅ or Sb₂O₅ segregation into TiO₂ occurred. Similarly, the XRD measurements did not show any additional peaks either, other than those for the anatase phase, which attains evidence for the absence of secondary or mixed phases.

4.4.3 Surface Area and Pore Size Analysis of TiO₂ and Doped TiO₂

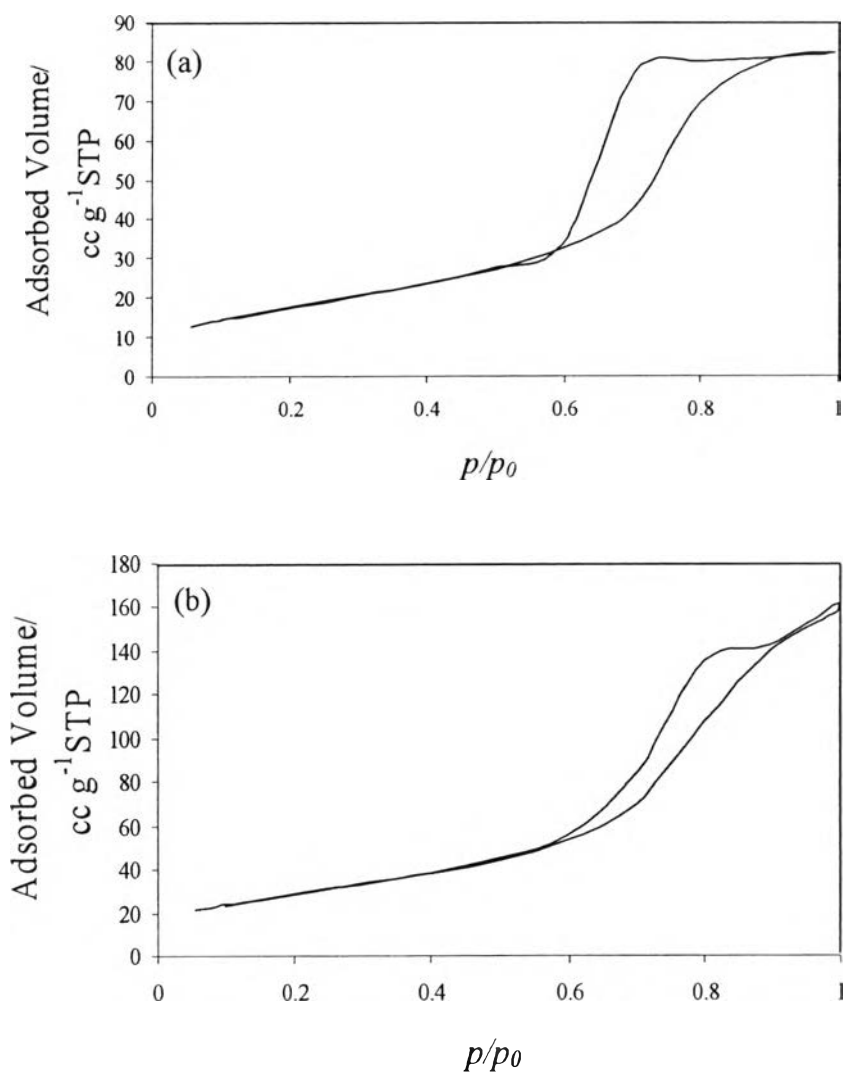
Particles

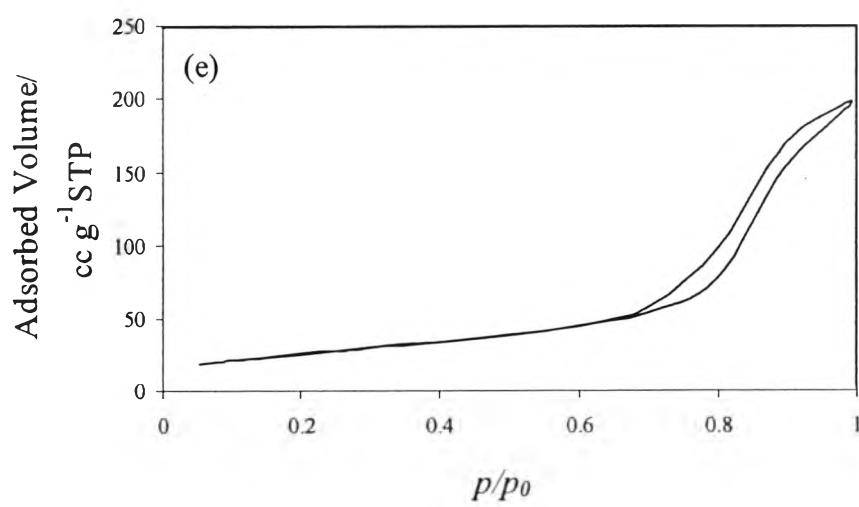
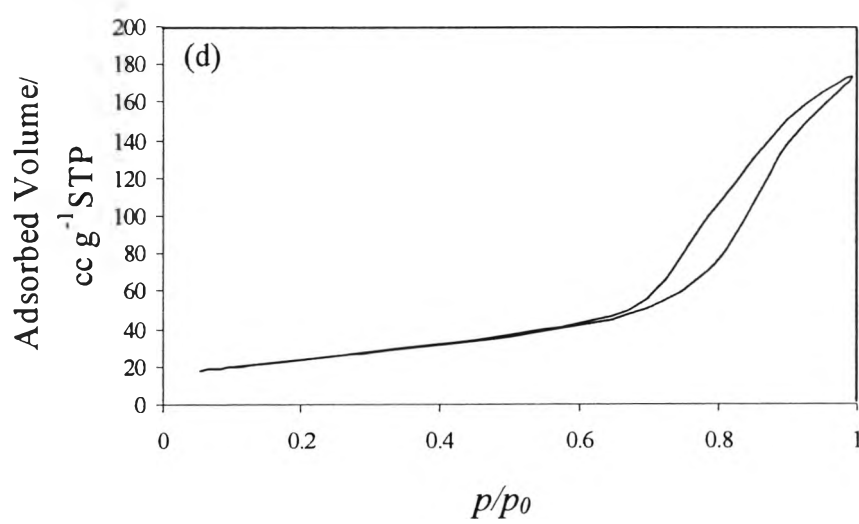
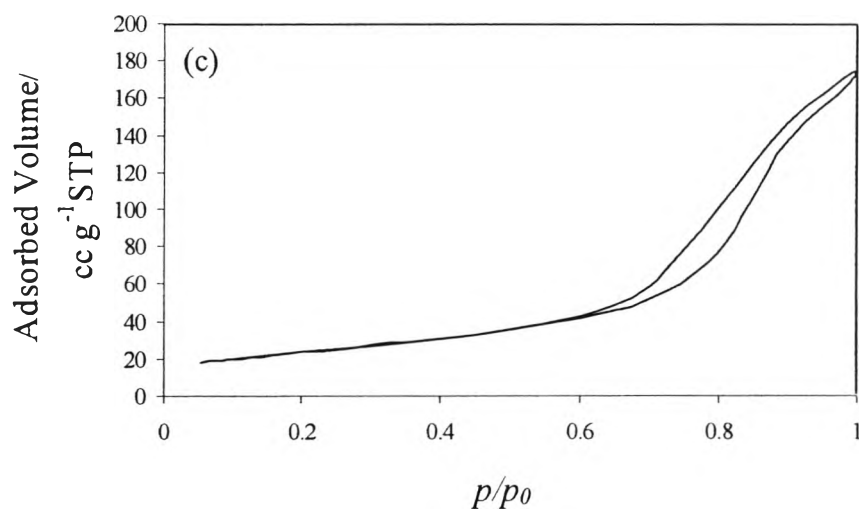
The results from the surface area, pore size and pore volume measurement of TiO₂ and doped TiO₂ after calcinations at 500 °C were summarized in Table 4.2. The materials present type IV of N₂ adsorption-desorption isotherms with hysteresis loops in Fig. 4.3, clearly indicating the mesoporous nature of TiO₂ and doped TiO₂ samples. The volume adsorbed for all isotherms sharply increased at high relative pressure (P/P_0), representing capillary condensation of nitrogen within the irregular mesopore structure.

Table 4.2 Physicochemical Properties of TiO₂ and doped TiO₂ Samples Calcined at 500 °C

Samples	S_{BET} (m ² g ⁻¹)	D_{Pore} (nm)	V_{Pore} (cc g ⁻¹)
TiO ₂	73.84	6.146	12.68
3 wt%Sb-TiO ₂	117.70	6.177	24.22
3 wt%Nb-TiO ₂	90.64	8.901	26.00
3 wt%Nb-1 wt%Sb-TiO ₂	92.02	8.830	26.39
3 wt%Nb-2 wt%Sb-TiO ₂	99.16	8.926	30.03
3 wt%Nb-3 wt%Sb-TiO ₂	99.55	8.909	27.73

As it can be seen in Table 4.2, the specific surface areas of doped TiO_2 were higher than that of pure TiO_2 . This increase may be due to the presence of Nb^{5+} and Sb^{5+} on the surface of TiO_2 which inhibits densification and crystalline growth of TiO_2 nanoparticles by providing dissimilar boundaries [15]. It is worth pointing out that the doping of antimony affects surface areas more than the doping of niobium in TiO_2 and the surface areas of antimony/niobium doped TiO_2 were increased by increasing the amount of antimony. This may be due to the more difference of ionic radius between titanium (IV) and antimony (V). The pore size distributions (PSDs) obtained using the Barrett-Joyner-Halenda (BJH) technique in the mesopore range for TiO_2 and doped TiO_2 are shown broad pore size distribution, as presented in Figure 4.4.





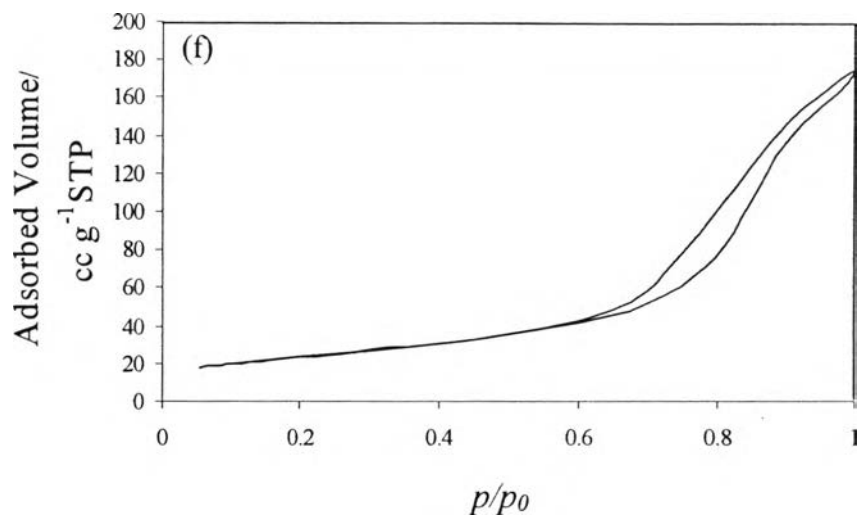
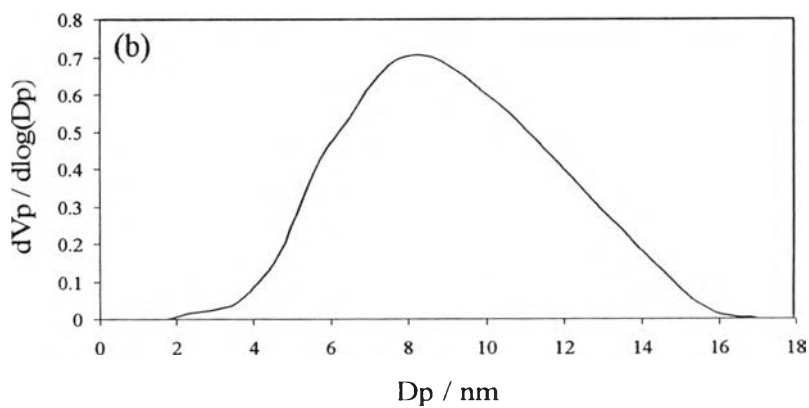
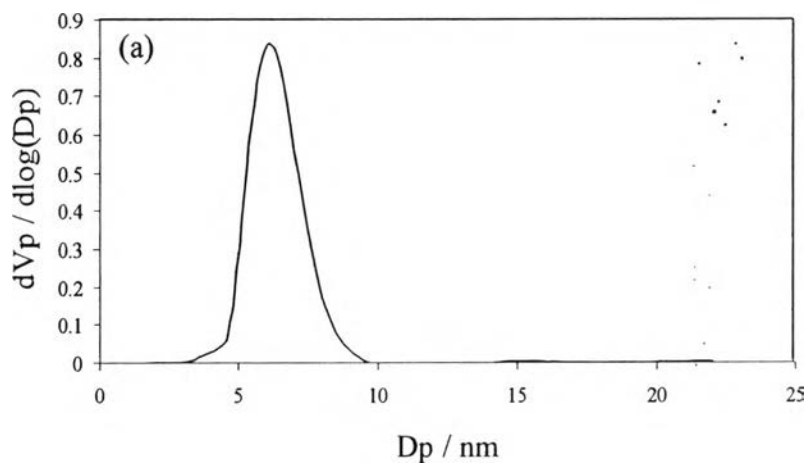
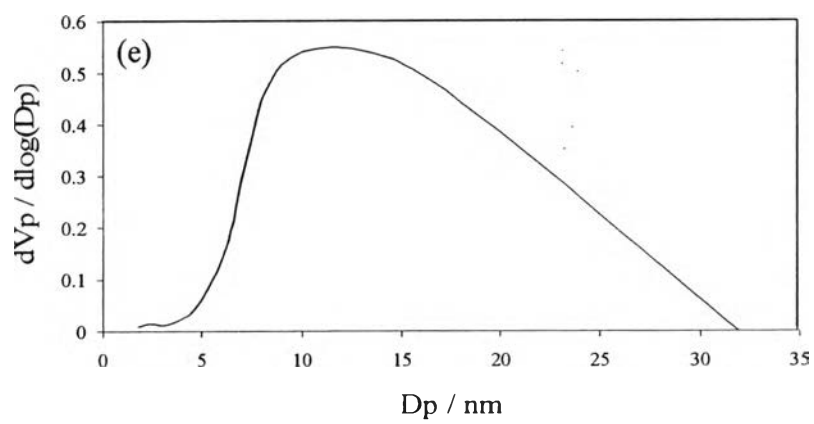
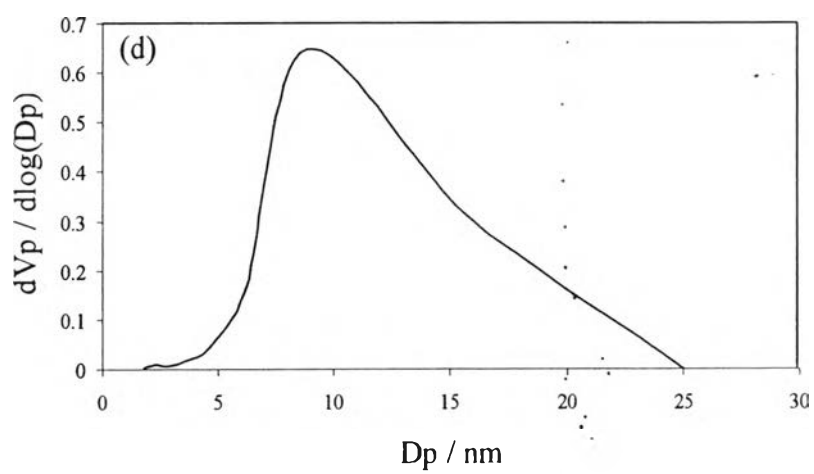
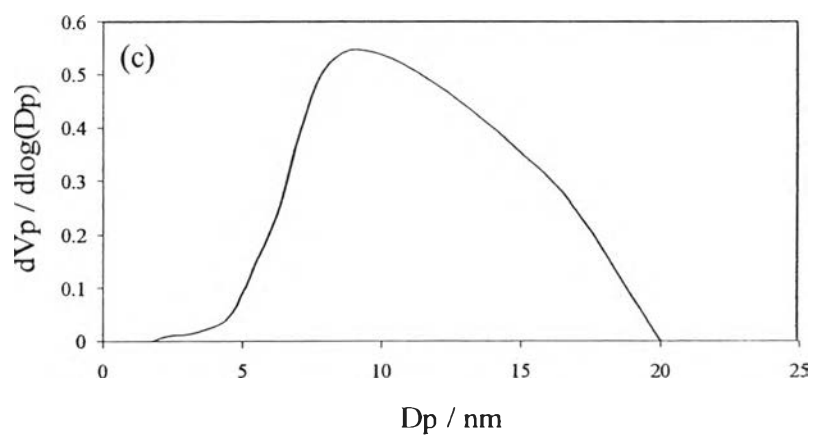


Figure 4.3 N_2 adsorption-desorption isotherms of (a) TiO_2 , (b) 3wt% $Sb-TiO_2$, (c) 3wt% $Nb-TiO_2$, (d) 3wt% $Nb-1wt\%Sb-TiO_2$, (e) 3wt% $Nb-2wt\%Sb-TiO_2$, (f) 3wt% $Nb-3wt\%Sb-TiO_2$ samples calcined at $500^\circ C$.





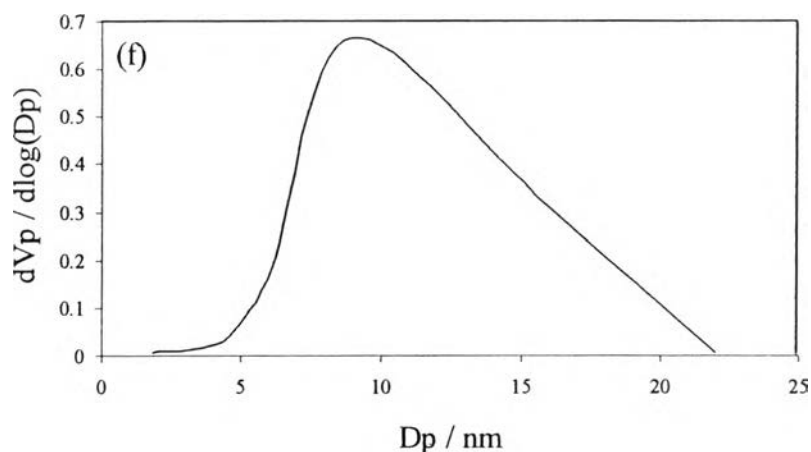


Figure 4.4 Pore size distribution of (a) TiO_2 , (b) 3wt% Sb-TiO_2 , (c) 3wt% Nb-TiO_2 , (d) 3wt% $\text{Nb-1wt}\%\text{Sb-TiO}_2$, (e) 3wt% $\text{Nb-2wt}\%\text{Sb-TiO}_2$, (f) 3wt% $\text{Nb-3wt}\%\text{Sb-TiO}_2$ samples calcined at 500°C .

4.4.4 TEM Analysis of TiO_2 and Doped TiO_2 Particles

TEM observation confirms XRD results that both Nb and/or Sb-doped and pure TiO_2 powders have uniform morphology in the anatase structure. The range of size is from 10 to 30 nm. The pure and doped TiO_2 crystallite size measured from the TEM images were similar to that calculated from the XRD data. All of the samples show high crystallinity with the characteristic d-spacing of 3.52 \AA corresponding to anatase phase, as indicated in Fig. 4.5 and Fig. 4.6, respectively.

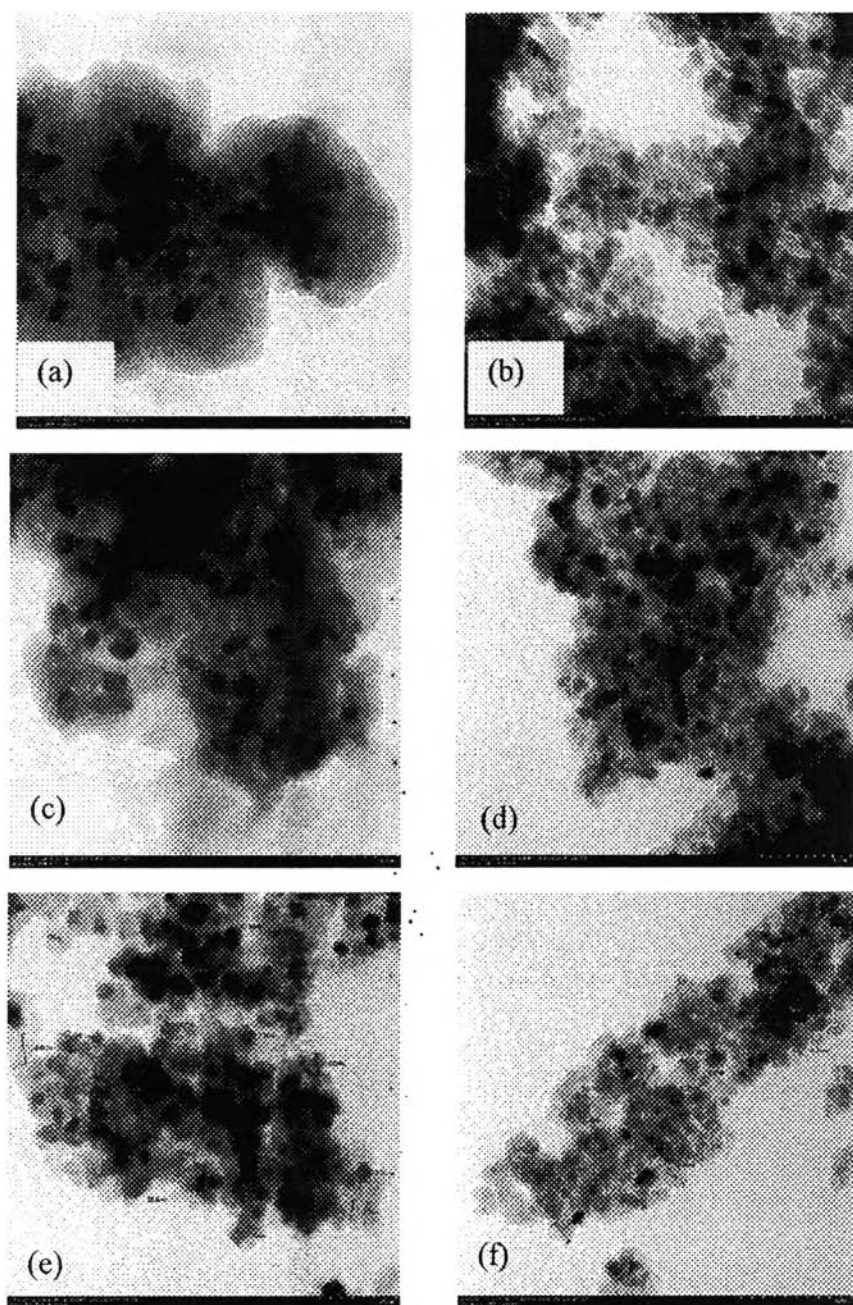


Figure 4.5 TEM images (scale bar = 100 nm) of (a) TiO_2 , (b) 3wt% Sb-TiO_2 , (c) 3wt% Nb-TiO_2 , (d) 3wt% $\text{Nb-1wt}\%\text{Sb-TiO}_2$, (e) 3wt% $\text{Nb-2wt}\%\text{Sb-TiO}_2$, (f) 3wt% $\text{Nb-3wt}\%\text{Sb-TiO}_2$ samples calcined at 500°C.

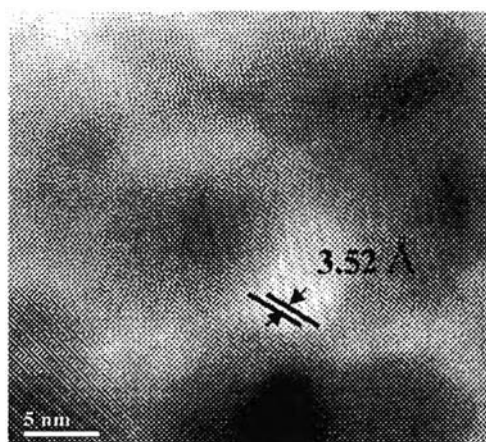


Figure 4.6 Lattice images (scale bar = 5 nm) of TiO₂ sample calcined at 500°C.

Moreover, the selected TEM images in Fig. 4.7 show pore characteristic of nanoparticles, which were agreed well with the BET surface area and BJH pore size analysis.

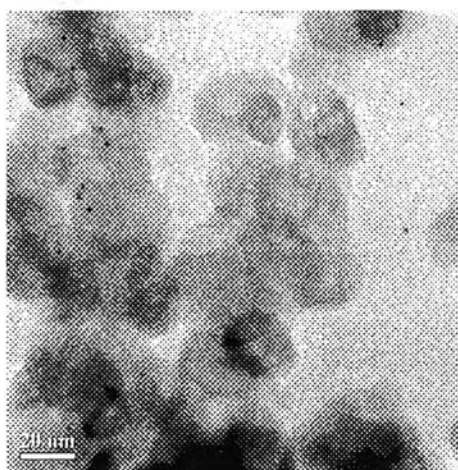


Figure 4.7 TEM image (scale bar = 20 nm) of 3wt%Nb-TiO₂ calcined at 500°C.

4.4.5 SEM/EDX Analysis of TiO₂ and Doped TiO₂ Particles

SEM photographs of particles obtained present spherical morphology of pure and doped TiO₂ nanoparticles and it was not significantly changed according to the introduction of Sb and Nb dopant as shown in Fig. 4.8.

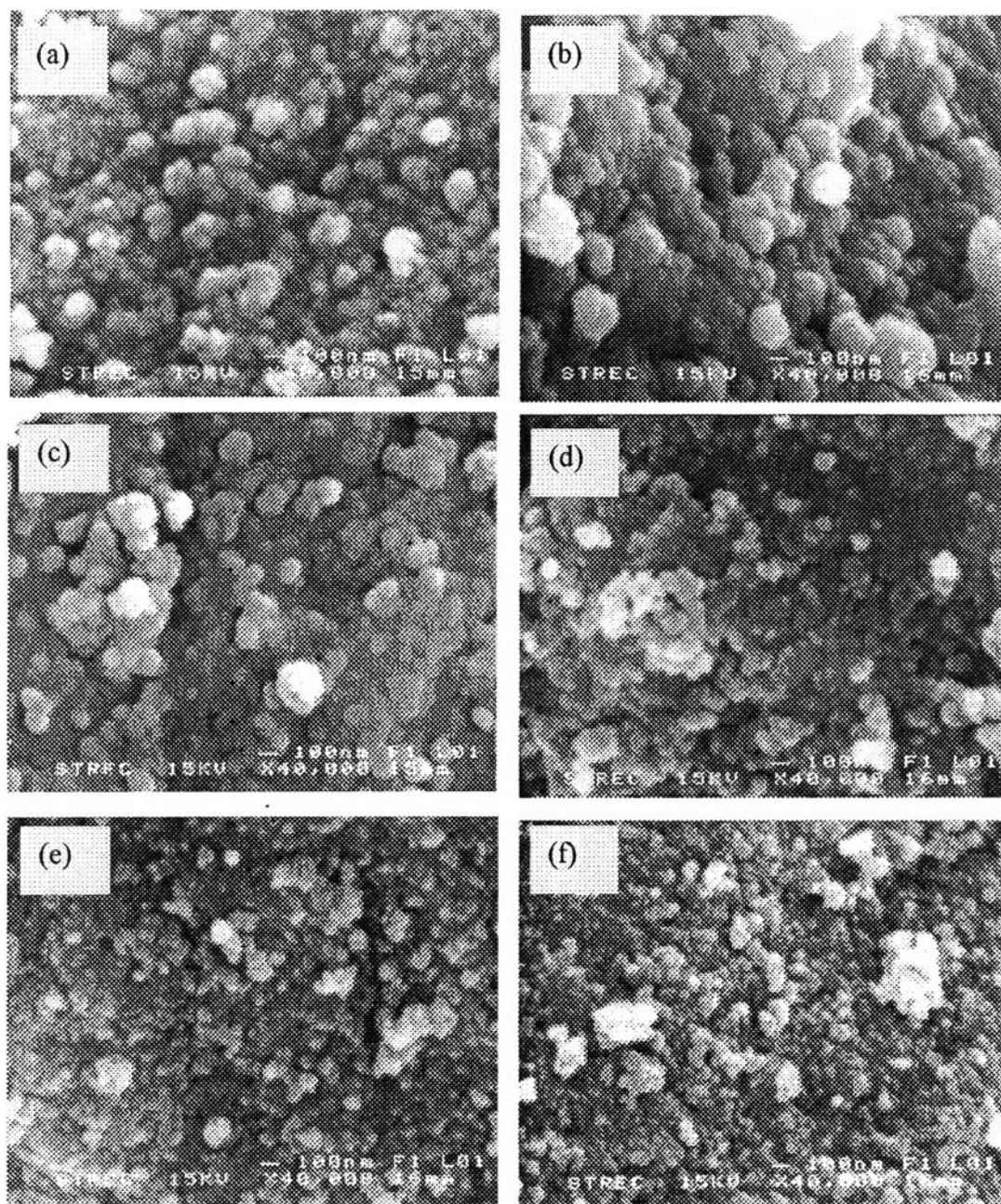
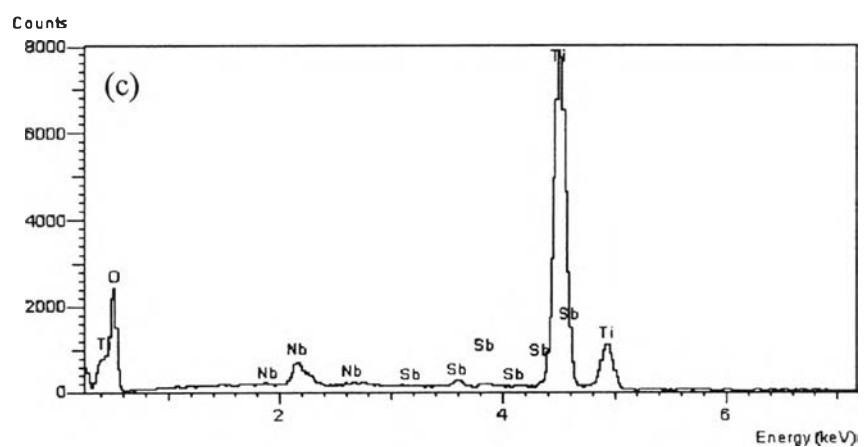
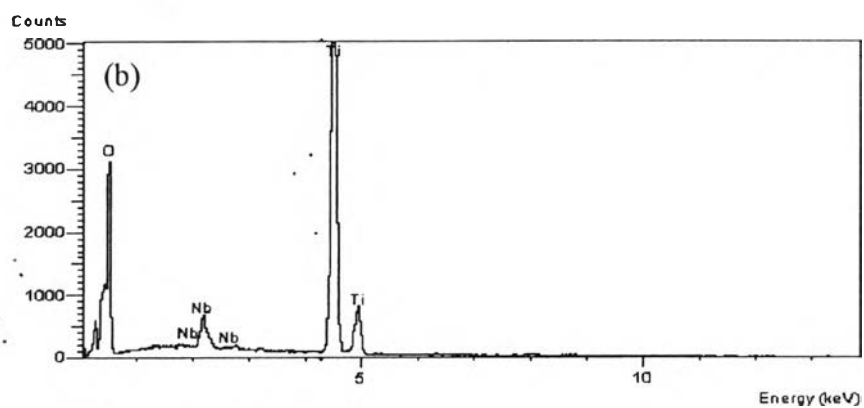
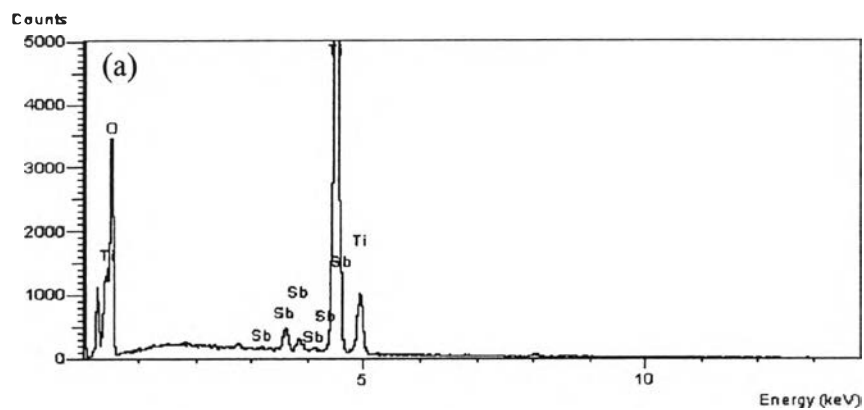


Figure 4.8 SEM images (scale bar = 100 nm) of (a) TiO_2 , (b) 3wt%Sb- TiO_2 , (c) 3wt%Nb- TiO_2 , (d) 3wt%Nb-1wt%Sb- TiO_2 , (e) 3wt%Nb-2wt%Sb- TiO_2 , (f) 3wt%Nb-3wt%Sb- TiO_2 samples calcined at 500°C.

In order to identify the presence of Nb^{5+} and Sb^{5+} ions in the TiO_2 matrix, EDX spectrum was carried out. The EDX spectrum shown in Fig. 4.9 confirmed that most of Nb^{5+} and Sb^{5+} ions can incorporate into the framework of

TiO₂ and substitute for the Ti⁴⁺ sites. Moreover, the results suggested that Nb and Sb were incorporated into the TiO₂ crystal because any peak corresponding to Nb and Sb-related compounds was not detected by X-ray diffraction patterns [16].



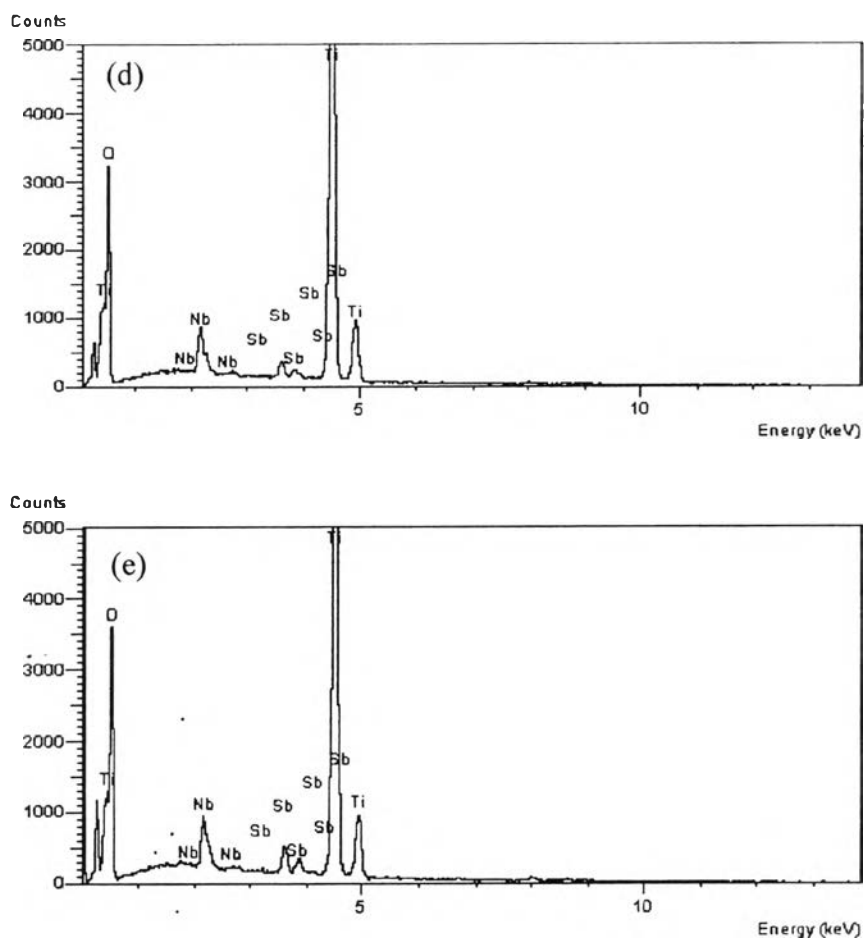


Figure 4.9 EDX graphs of (a) 3wt%Sb-TiO₂, (b) 3wt%Nb-TiO₂, (c) 3wt%Nb-1wt%Sb-TiO₂, (d) 3wt%Nb-2wt%Sb-TiO₂, (e) 3wt%Nb-3wt%Sb-TiO₂ samples calcined at 500°C.

In addition, EDX analysis was used to observe the distribution of Nb⁵⁺ and Sb⁵⁺ ions in the TiO₂ matrix. EDX Nb and/or Sb-mapping photographs show the homogenous and uniform distribution of Nb⁵⁺ and Sb⁵⁺ ions in the TiO₂ matrix as presented in Fig. 4.10.

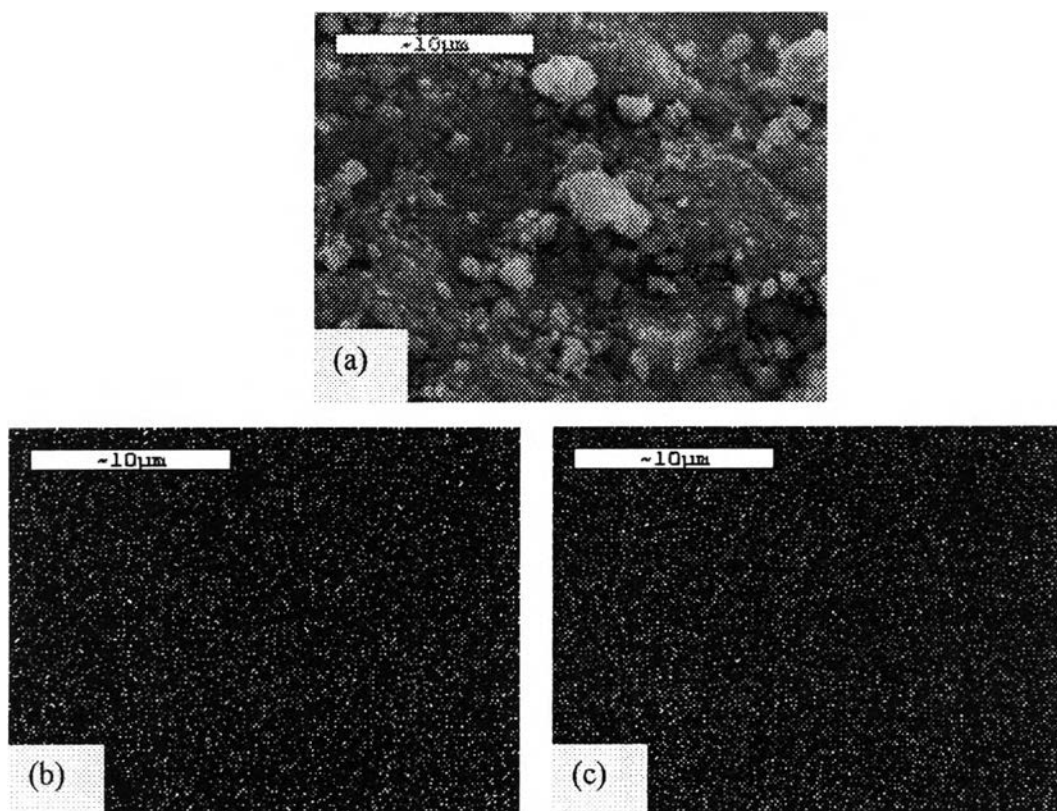


Figure 4.10 (a) SEM image (scale bar = 10 μm), (b) EDX Sb-mapping photograph, (c) EDX Nb-mapping photograph of 3wt%Nb-3wt%Sb-TiO₂ particles.

4.4.6 TGA Analysis of TiO₂/Epoxy and Doped TiO₂/Epoxy Thin Films

The hydration effect and thermal stability of thin films were also examined using TGA analysis. As shown in Fig.4.11, the mass loss for all of the samples occurs in 2 steps in a wide temperature range from room temperature range to 800°C. It can be observed that the relative mass decayed at temperature below 150°C and another mass loss is at approximately below 400°C. The first mass loss indicates the presence of water, while the second one presents the decomposition of epoxy binder. It is interesting to note that the mass loss of doped TiO₂/epoxy thin films (~10% mass loss) at temperature period for fuel cell operation (below 200°C) decayed more than that of pure TiO₂/epoxy thin film (~5% mass loss). Therefore, the doped TiO₂/epoxy thin films have higher water adsorption ability than pure TiO₂/epoxy thin film. Moreover, there was no significant shift of TGA thermographs

among doped TiO_2 /epoxy thin films. Therefore, this suggested that the amount of Sb dopant does not influence the degradation of thin films. Furthermore, all of the thin films also show good thermal stability. It can imply that the doped TiO_2 /epoxy thin films have some characteristics to use as membrane operated at high temperature in fuel cell application.

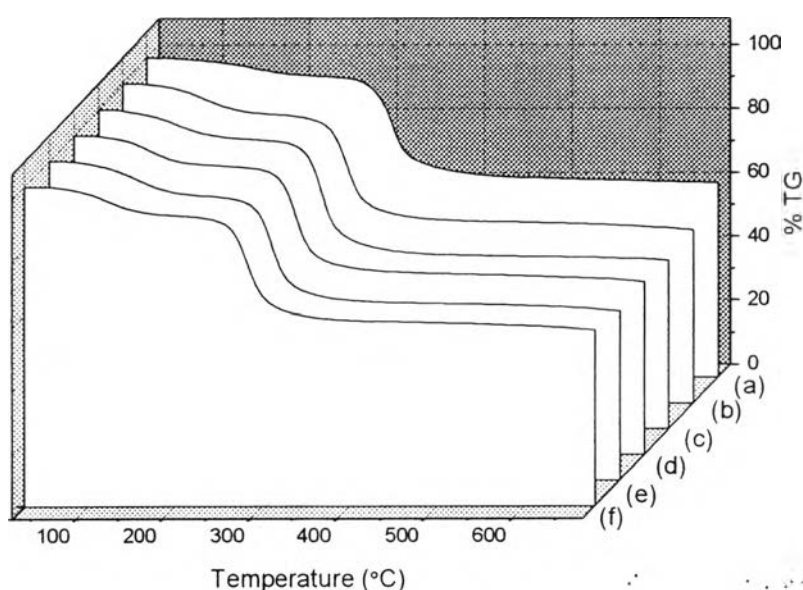


Figure 4.11 TGA thermograms of (a) TiO_2 /epoxy, (b) 3wt%Sb- TiO_2 /epoxy, (c) 3wt%Nb- TiO_2 /epoxy, (d) 3wt%Nb-1wt%Sb- TiO_2 /epoxy, (e) 3wt%Nb-2wt%Sb- TiO_2 /epoxy, (f) 3wt%Nb-3wt%Sb- TiO_2 /epoxy thin films.

4.4.7 SEM/EDX Analysis of TiO_2 /Epoxy Thin Film

SEM analysis was carried out in order to observe the thickness of thin film and the distribution of TiO_2 and epoxy binder. SEM image in Fig.4.12 revealed that the thickness of thin film is about 114 μm and the distribution of TiO_2 and epoxy is homogenous and uniform without any void inside the film. Because the main component is the ceramic powders and epoxy resin is only used as a binder, most ceramic part would be observed inside the thin film.

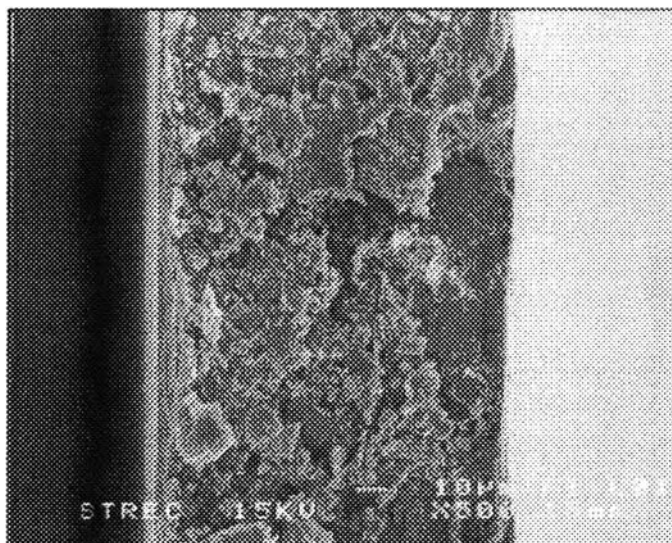


Figure 4.12 SEM image (scale bar = 10 μm) of cross-section area TiO₂/epoxy film.

The distribution and dispersion of the ceramic powders were confirmed by using EDX Ti-mapping photograph. The global distribution of TiO₂ is good but the specific areas have some agglomerations. Because of without gold coating, SEM micrograph had some charging in the picture.

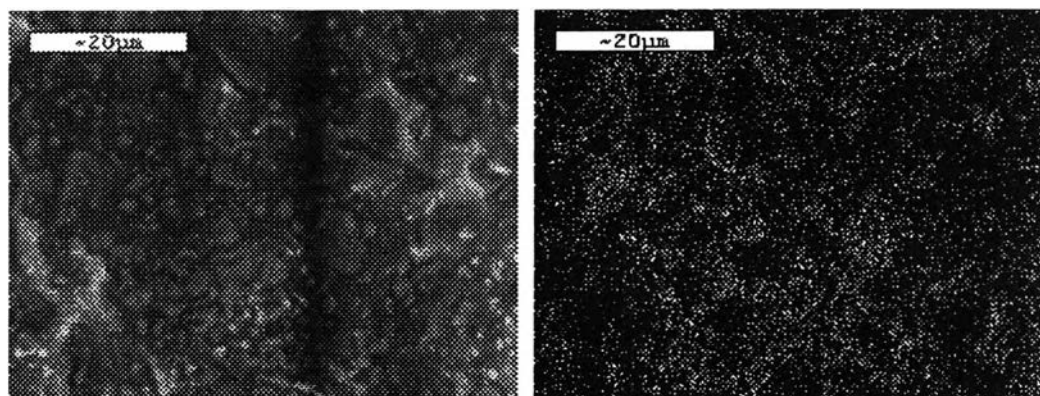


Figure 4.13 (a) SEM image (scale bar = 20 μm), (b) EDX Ti-mapping photograph of 3wt%Nb-3wt%Sb-TiO₂ particles/epoxy thin film.

4.4.8 Mechanical Properties of TiO₂ /Epoxy and Doped TiO₂ /Epoxy Thin films

Tensile properties were measured in order to evaluate the stiffness and strength of the thin films. As it can be seen in the Table 4.3, The TiO₂ /epoxy and doped TiO₂ /epoxy thin films have Young's Modulus and tensile strength better than the neat epoxy. This may be due to the high modulus of ceramic and the improvement of the interfacial interaction, especially epoxy and nano-ceramic particles are incorporated. The physiochemical entanglement between the polymer and the nano-particles causes effective interfacial bonding. The strong filler/matrix adhesion would lead to higher strength of the nanocomposite. On the other hand, the percentage of elongation-to-break of the neat epoxy is higher than the nanocomposite films because the chain flexibility of the crosslinked polymer on the nanocomposites is restricted [17].

Table 4.3 Mechanical Properties of TiO₂ /epoxy and doped TiO₂ /epoxy thin films

Sample	Young's Modulus (MPa)	Stress at Break (MPa)	Percentage Strain at Break
Epoxy	2314.43	12.96	31.02
TiO ₂ /Epoxy	3220.36	19.66	1.28
3 wt%Sb-TiO ₂ /Epoxy	2655.17	19.59	4.04
3 wt%Nb-TiO ₂ /Epoxy	2290.35	18.32	2.84
3 wt%Nb-1 wt%Sb-TiO ₂ /Epoxy	2590.40	17.14	1.89
3 wt%Nb-2 wt%Sb-TiO ₂ /Epoxy	3098.72	15.71	1.06
3 wt%Nb-3 wt%Sb-TiO ₂ /Epoxy	2725.48	12.34	3.79

4.4.9 Water Leakage Testing of TiO₂ /Epoxy and doped TiO₂ /Epoxy Thin films

Water leakage of all membranes was measured by pressing membranes into deionized water and then observing bubbles occurred. No bubbles occurred after pressing all of them into deionized water. This revealed that water cannot leak through all of the membranes.

Table 4.4 Water leakage of TiO₂ /epoxy and doped TiO₂ /epoxy thin films

(● = bubble occurred, × = no bubble)

Sample	1	2	3	4	5
Epoxy	×	×	×	×	×
TiO ₂ /Epoxy	×	×	×	×	×
3 wt%Sb-TiO ₂ /Epoxy	×	×	×	×	×
3 wt%Nb-TiO ₂ /Epoxy	×	×	×	×	×
3 wt%Nb-1 wt%Sb-TiO ₂ /Epoxy	×	×	×	×	×
3 wt%Nb-2 wt%Sb-TiO ₂ /Epoxy	×	×	×	×	×
3 wt%Nb-3 wt%Sb-TiO ₂ /Epoxy	×	×	×	×	×

4.4.10 Water Uptake Testing of TiO₂ /Epoxy and Doped TiO₂ /Epoxy Thin Films

The results of water uptake testing at room temperature exhibit that nano-composite films have higher percentage of water uptake than epoxy films because of the hydrophilicity of the ceramics and the doped TiO₂/epoxy films possess higher percentage of water uptake than TiO₂/epoxy films, which is agreed well with the TGA studied, as shown in Table 4.5. This increase may be due to the higher specific surface areas of doped TiO₂ ceramics than pure TiO₂ ceramics, according to the results from surface area measurement.

4.4.11 Proton Conductivity Measurement of TiO₂ /Epoxy and Doped TiO₂ /Epoxy Thin Films

The results of proton conductivity measurement of all of the membranes at room temperature were demonstrated in Table 4.5. The proton conductivity value of TiO₂/epoxy membrane was enhanced by doping niobium and antimony into TiO₂ matrix because the doped TiO₂ showed higher specific surface areas, leading to obtain higher water adsorption ability, and the porous surface condition of the TiO₂ ceramic particles was improved by doping antimony. High

surface areas and the acidic porous surface condition of the ceramic particles cause easier proton hopping, resulting in an increase of proton conductivity value.

Table 4.5 Water uptake (%) and proton conductivity of TiO₂/epoxy and doped TiO₂/epoxy thin films (- refers to not measured samples)

Sample	Percentage of water uptake	Proton conductivity, S cm ⁻¹
Epoxy	2.45	-
TiO ₂ /Epoxy	5.35	3.8 x 10 ⁻⁴
3 wt%Sb-TiO ₂ /Epoxy	9.65	-
3 wt%Nb-TiO ₂ /Epoxy	7.93	3.9 x 10 ⁻⁴
3 wt%Nb-1 wt%Sb-TiO ₂ /Epoxy	8.32	5.2 x 10 ⁻⁴
3 wt%Nb-2 wt%Sb-TiO ₂ /Epoxy	10.35	-
3 wt%Nb-3 wt%Sb-TiO ₂ /Epoxy	11.09	-

4.4.12 Hydrogen Transfer Mechanism via Single Fuel Cell Test Station

The 3 wt.%Sb-3 wt.%Nb-TiO₂/epoxy membrane was tested in a single fuel cell in the range of temperature 25-100°C with 100%RH. This membrane presented lower value (~ -0.895 V) although the thickness of 90 μm, probably the presence of an excess of inorganic material, weakens the structure of the polymer matrix and lower water adsorption ability comparing with Nafion. This low value of OCV has a consequence on the performance at all the investigated temperatures. However, the behavior of the OCV as a function of temperature showed that the OCV increases up to -0.063 V with cell temperature increasing. This increase may be due to the increasing of hydrogen transfer ability and the decreasing of electron moving ability. In order to enhance fuel cell performance, the other types of a binder and the varied content of ceramic powders should be tested so as to increase hydrogen transfer ability and water adsorption ability of membranes. Moreover, the higher operating temperature should be used in order to increase hydrogen transfer ability.

4.5 Conclusions

The results of this work show that pure TiO_2 and doped TiO_2 nanoparticles which were prepared using the sol-gel process present anatase phase with mesoporosity. As it can be seen from XRD and Raman results, the structure of doped TiO_2 samples was not significantly changed or distorted from anatase structure of pure TiO_2 and both Nb and Sb dopant were incorporated into the TiO_2 crystal according to EDX analysis. The specific surface areas of doped TiO_2 are higher than that of pure TiO_2 and it is worth pointing out that the doping of antimony affects surface areas more than the doping of niobium in TiO_2 , leading to the surface areas of doped TiO_2 enhanced by increasing the amount of Sb dopant. From TEM and SEM/EDX analysis, all of the samples are spherical morphology and both Nb and Sb dopant show good distribution in TiO_2 . All of the ceramics were fabricated into thin films and characterized. From TGA results, it can be concluded that the doped TiO_2 /epoxy films possess good thermal stability and have higher water adsorption ability than TiO_2 /epoxy film. Furthermore, the nanocomposite films exhibit good tensile modulus and strength because the ceramic powders show good distribution in the films, corresponding with SEM/EDX micrograph. The proton conductivity value of TiO_2 /epoxy membrane was enhanced by doping niobium and antimony into TiO_2 matrix. These imply that these samples have some characteristics to use as a membrane operated at high temperature in fuel cell applications.

4.6 Acknowledgements

The author is grateful for the scholarship and funding of the thesis work provided by the Petroleum and Petrochemical College; the National Excellence Center for Petroleum, Petrochemicals, and Advanced Materials, Thailand. The author acknowledges Hitachi Hi-Technologies Corporation for the morphological characterization using TEM zero A H-7650.

4.7 References

- [1] Colomer, M.T. (2005) Nanoporous anatase ceramic membranes as fast-proton-conducting materials. Journal of the European Ceramic Society, xxx, xxx-xxx.
- [2] Vichi, F.M., Tejedor-Tejedor, M.I., and Anderson, M.A. (2000) Effect of pore wall chemistry on proton conductivity in mesoporous titanium dioxide. Chem. Mater., 12, 1762-1770.
- [3] Vichi, F.M., Tejedor-Tejedor, M.I., and Anderson, M.A. (2005) Proton conductivity in tungsten and antimony-modified titania ceramics prepared by the sol-gel method. Solid State Ionics, 176, 973-978.
- [4] Ekström, H., Wickman, B., Gustavsson, M., and Hanarp, P. (2007) Nanometer-thick films of titanium oxide acting as electrolyte in the polymer electrolyte fuel cell. Electrochimica Acta, 52, 4239-4245.
- [5] Jalani, N.H., Dunn, K., and Datta, R. (2005) Synthesis and characterization of Nafion[®]-MO₂ (M=Zr, Si, Ti) nanocomposite membranes for higher temperature PEM fuel cells. Electrochimica Acta, 51, 553-560.
- [6] Saccà, A., Carbone, A., Passalacqua, E., D'Epifanio, A., Licocchia, S., Traversa, E., Sala, E., Traini, F., and Ornelas, R. (2005) Nafion-TiO₂ hybrid membranes for medium temperature polymer electrolyte fuel cells. Journal of Power Sources, 152, 16-21.
- [7] Shao, Z.G., Xu, H., Li, M., and Hsing, I.M. (2006) Hybrid Nafion-inorganic oxides membrane doped with heteropolyacids for high temperature operation of proton exchange membrane fuel cell. Solid State Ionics, 177, 779-785.
- [8] Kim, Y.M., Choia, S.H., Leea, H.C., Honga, M.Z., Kima, K., and Leeb, Ho-In (2004) Organic-inorganic composite membranes as addition of SiO₂ for high temperature-operation in polymer electrolyte membrane fuel cells (PEMFCs). Electrochimica Acta, 49, 4787-4796.
- [9] Saccà, A., Gatto, I., Carbone, A., Pedicini, R., and Passalacqua, E. (2006) ZrO₂-Nafion composite membranes for polymer electrolyte fuel cells (PEMFCs) at intermediate temperature. Journal of Power Sources, 163, 47-51.

- [10] Ahmad, A., Thiel, J., and Shah, S. (2007) Structure effects of niobium and silver doping on titanium dioxide nanoparticles. Journal of Physics: Conference Series, 61, 11-15.
- [11] Xu, J., Jia, C., Cao, B., Zhang, W.F. (2007) Electrochemical properties of anatase TiO₂ nanotubes as an anode material for lithium-ion batteries. Electrochimica Acta, 52, 8044–8047.
- [12] Lee, J.E., Oh, S.M., and Park, D.W. (2004) Synthesis of nano-sized Al doped TiO₂ powders using thermal plasma. Thin Solid Films, 457, 230–234.
- [13] Chen, D., Jiang, Z., Geng, J., Wang, Q., and Yang, D. (2007) Carbon and Nitrogen Co-doped TiO₂ with Enhanced Visible-Light Photocatalytic Activity. Ind. Eng. Chem. Res., 46, 2741-2746.
- [14] Hirano, M. and Matsushima, K. (2006) Photoactive and Adsorptive Niobium-Doped Anatase (TiO₂) Nanoparticles: Influence of Hydrothermal Conditions on their Morphology, Structure, and Properties. J. Am. Ceram. Soc., 89, 110–117.
- [15] Venkatachalam, N., Palanichamy, M., Arabindoo, B., Murugesan, V. (2007) Enhanced photocatalytic degradation of 4-chlorophenol by Zr⁴⁺ doped nano TiO₂. Journal of Molecular Catalysis A: Chemical 266, 158–165.
- [16] Jing, D., Zhang, Y., and Guo, L. (2005) Study on the synthesis of Ni doped mesoporous TiO₂ and its photocatalytic activity for hydrogen evolution in aqueous methanol solution. Chemical Physics Letters, 415, 74–78.
- [17] Chatterjee, A., Islam, M.S. (2008) Fabrication and characterization of TiO₂-epoxy nanocomposite. Materials Science and Engineering A xxx, xxx–xxx.